CAMBRIDGE UNIVERSITY PRESS

RESEARCH ARTICLE

Design and analysis of pipeline inspection robot based on generalized parallel mechanisms

Yongheng Xing^{1,†}, Weizhan Ma^{1,†}, Chunxu Tian¹ and Dan Zhang²

Received: 24 April 2025; Revised: 30 August 2025; Accepted: 4 September 2025; First published online: 13 October 2025

Keywords: parallel mechanism; structure synthesis; screw theory; topological graph; motion/force transmission

Abstract

Pipeline inspection robots play a crucial role in maintaining the integrity of pipeline systems across various industries. In this paper, a novel pipeline inspection robot is designed based on a four degrees-of-freedom (DOF) generalized parallel mechanism (GPM). First, a four DOF mechanism is introduced using numerical and graph synthesis. The design employs numerical and graph synthesis methods to achieve an ideal symmetric configuration, enhancing the robot's adaptability and mobility. The coupling mid-platform, inspired by parallelogram mechanisms, enables synchronized contraction motion, allowing the robot to adjust to different pipe diameters. Then, the constraints of the pipeline inspection robot in the elbow are analyzed based on task requirements. Through kinematic and performance analyses using screw theory, the mechanism's feasibility in practical applications is confirmed. Theoretical analysis, simulations, and experiments demonstrate the robot's ability to achieve active steering in T-branches and elbows. Experimental validation in straight and bent pipes shows that the robot meets the expected speed targets and can successfully navigate complex pipeline environments. This research highlights the potential of GPMs in advancing the capabilities of pipeline inspection robots for real-world applications.

1. Introduction

Parallel mechanisms have garnered significant attention in various robotic applications due to their inherent advantages of high stiffness, precision, and load-bearing capacity [1]. These attributes make them particularly suitable for designing robots operating in challenging environments, such as pipeline inspection robots [2]. Traditional parallel mechanisms, derived from the Gough–Stewart platform, have been widely studied and applied [3, 4]. However, they often face limitations such as small workspace, limited working modes, and susceptibility to singular configurations. To address these issues, researchers have proposed generalized parallel mechanisms (GPMs) [5–8], which allow for coupled motion between kinematic chains. GPMs with coupling sub-chains offer enhanced overall stiffness and load-bearing capacity, making them promising candidates for complex robotic applications [9, 10].

As for the application of pipeline inspection robots, they must have the ability to navigate through various pipe configurations, including straight pipes, elbows, and T-branches. Existing pipeline inspection robots, such as wheeled [11], inchworm [12], and screw-type [13] designs, have demonstrated successful examples of traversing straight pipes. For the pipeline inspection robots with serial mechanisms, Tavakoli et al. [14] presented a Pole Climbing Robot (PCR) with a novel four degrees-of-freedom (4-DOF) series-connected rod-climbing mechanism, featuring a unique V-shaped holder and a fast

¹Institute of AI and Robotics, College of Intelligent Robotics and Advanced Manufacturing, Fudan University, Shanghai, PR China

²Department of Mechanical Engineering, The Hong Kong Polytechnic University, Hong Kong, PR China Corresponding authors: Chunxu Tian; Email: chxtian@fudan.edu.cn, Dan Zhang; Email: dan.zhang@polyu.edu.hk

[†]These authors contributed equally.

[©] The Author(s), 2025. Published by Cambridge University Press. This is an Open Access article, distributed under the terms of the Creative Commons Attribution licence (https://creativecommons.org/licenses/by/4.0/), which permits unrestricted re-use, distribution and reproduction, provided the original article is properly cited.

rotation mechanism for nondestructive testing (NDT) in industrial pipelines with bends and tees. Roh et al. [15] introduced a differential-drive pipeline robot designed to solve the problem of precise wheel speed control when moving inside urban gas pipelines, enabling efficient pipeline inspection. Li et al. [16] described the development of a pipeline inspection robot tailored for the standard oil pipelines of China National Petroleum Corporation, aiming to enhance inspection efficiency and safety. Kim et al. [17] proposed an in-pipe robot with a multiaxial differential gear mechanism to address the challenge of precise wheel speed control in pipe environments, improving the robot's stability and inspection accuracy.

However, the pipeline inspection robots based on serial mechanisms often struggle with complex pipe geometries. Existing pipeline inspection robots can pass through most horizontal straight pipes smoothly, while the pipes are not always straight. Applications of parallel mechanisms to pipeline robots can significantly improve their mobility and adaptability. For instance, Roslin et al. [18] presented a novel pipeline inspection robot with a hybrid locomotion system that combines the advantages of wheeled and tracked systems, enabling stable movement in various pipeline types and improving obstacle-crossing ability and inspection performance. Ismail et al. [19] described the development of a snake-like pipeline inspection robot with active wheels, designed to move flexibly in complex pipeline environments like a snake, which offered good mobility and adaptability for inspection tasks. Kwon et al. [20] developed a robot featuring a linkage-type mechanical clutch, enabling it to operate within pipelines of 100 mm diameter. It can move at 14 cm/s and navigate through 90-degree bends while detecting pipeline conditions. Shen et al. [2] presented the design of a parallel four-legged pipe robot based on a planar parallel structure for urban underground polyethylene pipelines. The structure and working principles are introduced, including a kinematic model, forward and inverse kinematic solutions, and motion simulations. Sakamoto et al. [21] designed a pipe diagnostic system to reduce inspection time and workload while enhancing diagnostic accuracy, featuring a pipe thickness measuring robot equipped with an ultrasonic probe for external pipe inspections.

Therefore, the structure of GPM with coupling sub-chains can be a potential choice to improve the kinematic performance of the pipeline inspection robots. Since they possess the following characteristics: the kinematic chains are not necessarily independent but may act on the moving platform in a coupled manner, significantly enhancing overall stiffness and load-bearing capacity. While most synthesis methods for GPMs with coupling sub-chains are based on graph theory. For instance, Tian et al. [22] divided the synthesis process of such coupled mechanisms into two parts: topological embryo graph synthesis and topological graph synthesis, resulting in the first synthesis of 33 new topological embryo graphs. Xia et al. [23, 24] provided the possible contracted graphs of the 6-DOF leg based on the number synthesis and graph synthesis method. Besides, Wu et al. [25] proposed a design method of a closed-chain leg inspired by the California mite. A legged robot equipped with multiple motors possessed a 71.7 % obstacle-to-leg-length ratio. Nevertheless, existing research on GPM with coupling sub-chains still faces limitations in applications. Applying it to pipeline robots can not only enhance the mechanism's stiffness, thereby extending its service life, but also improve the flexibility of such robots during operation.

In summary, this paper presents a novel pipeline inspection robot based on a 4-DOF GPM. The design leverages numerical and graph synthesis methods to achieve a symmetric configuration. The coupling mid-platform, inspired by parallelogram mechanisms, enables synchronized contraction motion, enhancing the robot's adaptability to different pipe diameters. Through kinematic and performance analysis using screw theory, the feasibility of the mechanism in practical applications is confirmed. Simulation and experimental results validate the robot's ability to achieve active steering in T-branches and its potential for real-world pipeline inspection tasks.

The following of this paper is organized as follows: In Section 2, it generates the topological structure of the pipeline robot using numerical and graph synthesis methods and incorporates motion characteristics into the diagram. Then, the coupling mid-platform based on the parallelogram mechanism is designed, and a 3D model of the overall mechanism is proposed. In Section 4, the closed-loop equations of the forward kinematics are first solved. Additionally, the performance analysis of the mechanism,

including stiffness, dexterity, and motion/force transmission, is introduced, and the velocity and contact force of the robot are analyzed. Afterward, the simulations of the pipeline inspection robot in elbow and T-branch scenarios are conducted. Finally, we design the prototype in detail, including the entire control system, and select three scenarios to conduct experiments, verifying the effectiveness and universality of the proposed mechanism.

2. Mechanism synthesis

Generally speaking, the topological structure of a GPM can be described using a topological graph. The topological graph of the mechanism can be obtained by methods such as number synthesis and numerical synthesis. For a GPM, the overall degrees of freedom can typically be defined as M, which can be calculated using the modified Kutzbach-Grübler [22]:

$$M = \sum_{i=1}^{j} F_i - d(J - N + 1) + v - z \tag{1}$$

where j represents the number of motion pairs, d denotes the motion dimension of the mechanism, F_i signifies DOF at i-th joints, J means the number of motion pairs with single-DOF, N indicates the number of basic links, and V represents the number of redundant constraints, which corresponds to the number of passive DOF.

In a mechanism, two-DOF motion pairs (such as U-joints and cylindrical joints) and three-DOF motion pairs (such as spherical joints) can be replaced by single-DOF motion pairs, respectively. Denote $n_k(k=2,3,\ldots,n)$ as the number of links with k-DOF. Then, denote $\sum_{k=2}^n n_k$ as the number of basic links and $\sum_{k=2}^n k \cdot n_k/2$ as the number of motion pairs. Thus, $\sum_{i=1}^j F_i$ can be expressed as follows:

$$\sum_{i=1}^{J} F_i = \frac{1}{2} (2n_2 + 3n_3 + 4n_4 + \ldots) = \frac{1}{2} \sum_{k=2}^{n} k \cdot n_k$$
 (2)

Combining (1) and (2), M can be obtained as

$$M = 6\left(\sum_{k=2}^{n} n_k - \frac{1}{2}\sum_{k=2}^{n} k \cdot n_k - 1\right) + \frac{1}{2}\sum_{k=2}^{n} k \cdot n_k + \nu - z$$
(3)

To calculate the number of independent loops in a topological graph, Euler's formula is widely applied. The following relationships can be obtained:

$$V = \frac{1}{2} \sum_{k=2}^{n} k \cdot n_k - \sum_{k=2}^{n} n_k + 1 = \frac{1}{2} (n_3 + 2n_4 + 3n_5 + 4n_6 + \dots) + 1$$
 (4)

From (4), binary links (links with two DOF) do not affect the number of independent loops. By substituting (4) into (3), the number of binary links can be expressed as follows:

$$n_2 = 6 + 5(V - 1) + M + z - v - \sum_{k=2}^{n} n_k = 5V - \sum_{k=2}^{n} n_k + \Phi$$
 (5)

where $\Phi = M + z - v + 1$ reflects the relationship between binary links and redundant constraints. The number synthesis of a GPM can be performed using Eq. (3)–(5) to determine the number and types of basic links in the mechanism.

Pipeline robots need to adapt to the radius of the pipeline and avoid obstacles. Therefore, it is assumed that the parallel pipeline robot in this paper has three basic kinematic chains, with variable positions between them, which requires a three-DOF mechanism to realize. In addition, to accommodate varying pipeline sizes, the robot is able to achieve diameter adjustment. Therefore, the expected number of DOF is four.

For a conventional parallel mechanism with four degrees of freedom and three kinematic chains, the number of independent loops is 2. However, due to coupling sub-chains or configurable platforms

								_			
No.	n_2	n_3	n_4	n_5	n_6	No.	n_2	n_3	n_4	n_5	n_6
1	$23 + \Phi$	12	0	0	0	18	$29 + \Phi$	3	0	3	0
2	$24 + \Phi$	10	1	0	0	19	$29 + \Phi$	3	1	1	1
3	$25 + \Phi$	9	0	1	0	20	$29 + \Phi$	2	3	0	1
4	$25 + \Phi$	8	2	0	0	21	$29 + \Phi$	2	2	2	0
5	$26 + \Phi$	8	0	0	1	22	$29 + \Phi$	1	4	1	0
6	$26 + \Phi$	7	1	1	0	23	$29 + \Phi$	0	6	0	0
7	$26 + \Phi$	6	3	0	0	24	$30 + \Phi$	2	1	0	2
8	$27 + \Phi$	6	1	0	1	25	$30 + \Phi$	2	0	2	1
9	$27 + \Phi$	6	0	2	0	26	$30 + \Phi$	1	2	1	1
10	$27 + \Phi$	5	2	1	0	27	$30 + \Phi$	1	1	3	0
11	$27 + \Phi$	4	4	0	0	28	$30 + \Phi$	0	4	0	1
12	$28 + \Phi$	5	0	1	1	29	$30 + \Phi$	0	3	2	0
13	$28 + \Phi$	4	2	0	1	30	$31 + \Phi$	1	0	1	2
14	$28 + \Phi$	4	1	2	0	31	$31 + \Phi$	0	2	0	2
15	$28 + \Phi$	3	3	1	0	32	$31 + \Phi$	0	1	2	1
16	$28 + \Phi$	2	5	0	0	33	$31 + \Phi$	0	0	4	0
17	$29 + \Phi$	4	0	0	2	34	$32 + \Phi$	0	0	0	3

Table I. Combination of basic links corresponding to V = 7.

in GPMs, the number of independent loops should exceed 2. The number of independent loops can significantly affect the performance of a mechanism. Generally, a mechanism tends to exhibit better stiffness characteristics with a larger V. Therefore, the number of independent loops can be selected as 7. Since the number of binary links B does not affect the loop, the topological graph can be represented by combinations of basic links such as ternary links T, quaternary links Q, pentagonal links P, and hexagonal links H. The combinations of basic links for different numbers of independent loops are shown in Table I.

In a topological graph, motion pairs are represented by vertices, and links are represented by edges, illustrating relationships between them. In topological graphs, the vertices representing the basic links H, Q, and T are connected by 6, 4, and 3 edges, respectively. In this paper, all vertices corresponding to the basic links are distributed on a circle, with each basic link consistently having two edges fixed on it. Configuration **No.** 20 from Table I is selected as the result of numerical synthesis, indicating that the mechanism includes 2 ternary links, 3 quaternary links, and 1 hexagonal link. Before constructing topological graphs, the six basic links need to be arranged. Then, six different arrangements can be obtained: HQQQTT, HQQTQT, HQQTQT, HQTQQT, HTQQQT, and HQTQTQ. To facilitate analysis and achieve balanced load distribution, the robot designed in this paper should possess a symmetric configuration. Therefore, this paper takes the HQTQTQ topological arrangement as an example to construct topological graphs.

The vertices representing the basic links H, Q, and T have 4, 2, and 1 undetermined edges, respectively. Classifying by the edge distribution of the basic link H, there are three cases: 1-1-1-1, 2-1-1, and 2-2. The corresponding topological graphs are shown in Figure 1.

If two topological graphs are symmetrically distributed, then they are isomorphic. In Figure 1, this situation has been excluded. Numbers 1-5 represent topological graphs whose edge distribution of the basic link H is 1-1-1-1. Similarly, numbers 6-21 and 22-23 represent cases where edge distributions of the basic link H are 2-1-1 and 2-2, respectively.

Since our robot only travels through regular pipes (e.g. round, square), this paper only considers symmetric topological configurations. So, only the topological graphs represented by numbers 5, 16, 17, 18, 19, and 23 in Figure 1 are valid. Take the topological graph numbered 18 as an example.

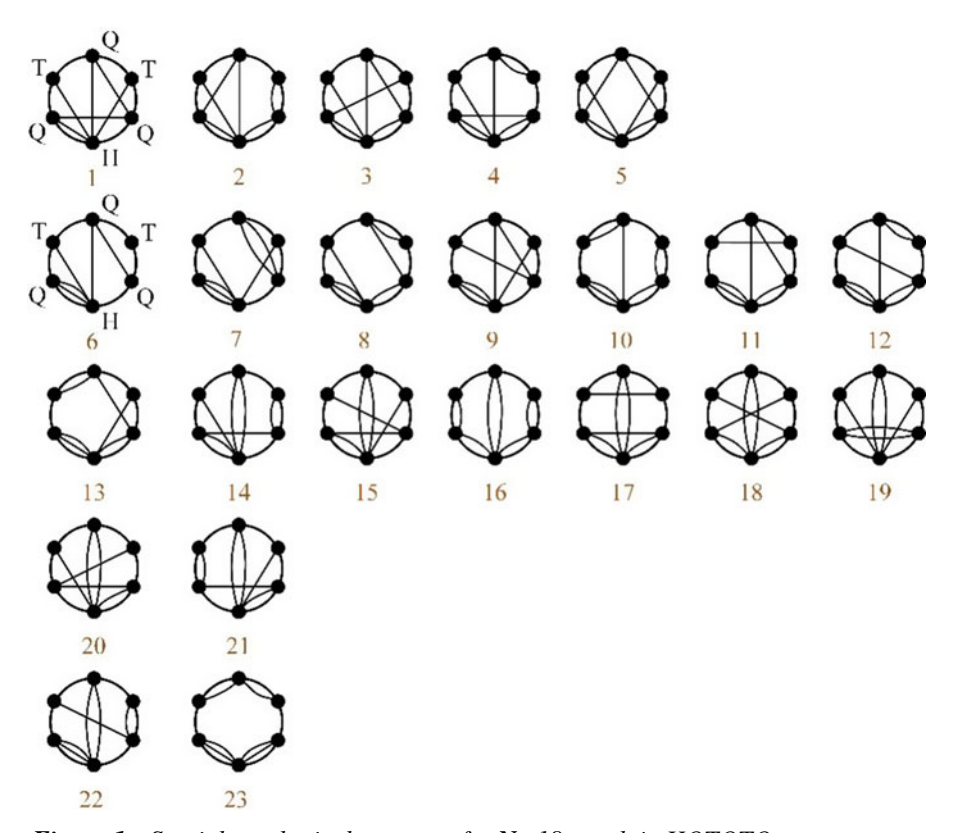


Figure 1. Spatial topological structure for No.18 graph in HQTQTQ arrangement.

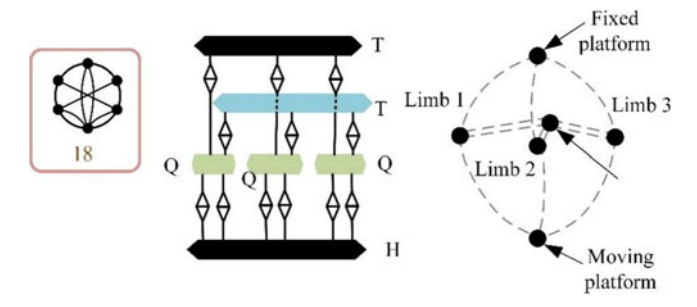


Figure 2. Topological structure.

The topological structure corresponding to this topological graph is shown in Figure 2. The two basic links T can be regarded as the moving platform and the fixed platform, respectively, while the three basic links Q represent the three topological kinematic chains. The basic link H provides the coupling relationship among the three chains. Therefore, this structure is a GPM with coupled kinematic limbs. Stretching it into three-dimensional space can more intuitively demonstrate its structural characteristics. In Figure 2, the mechanism is composed of a fixed platform, a moving platform, a mid-platform, and three chains.

To achieve obstacle avoidance within the pipeline, the position between the three kinematic limbs should be variable. This paper realizes it through three independent actuators. Three revolute joints are used to connect the fixed platform to the kinematic limbs, enabling independent rotational motion. Similarly, three passive revolute joints are placed at the connections between the moving platform and the kinematic limbs. Additionally, the pipeline robot should possess pipeline adaptability, meaning that

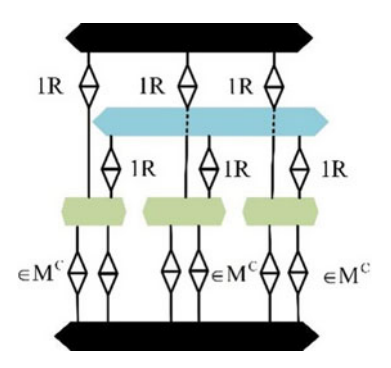


Figure 3. Movement diagram.

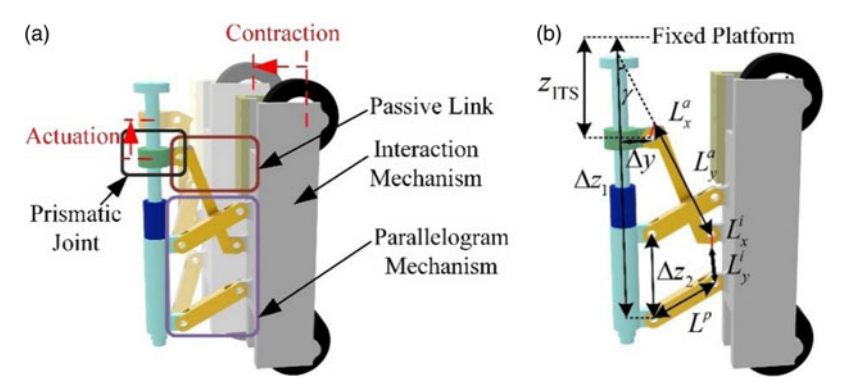


Figure 4. Design of the coupled mid platform: (a) Connection design. (b) Parameters in the mid platform.

the pipeline robot should synchronously achieve contraction or expansion. Denote this motion as M^{C} . Therefore, the only thing that remains to be determined is how to achieve synchronous motion through the coupling relationship of the three kinematic limbs. The movement diagram is shown in Figure 3.

3. Design of pipeline inspection robot

3.1. Design of the coupling mid platform

To achieve the contraction motion M^{C} , the mid platform and the chains should possess the movement DOF within a plane. Since using prismatic joints would significantly increase the size and weight of the mechanism, it is necessary to replace prismatic joints with revolute joints. In classical parallel mechanisms, a parallelogram mechanism can provide a translation DOF whose axis is perpendicular to one of its sides. Therefore, such sub-parallel mechanisms are introduced at the connection between the limbs and the mid-platform to achieve the contraction motion. Additionally, to realize synchronized contraction motion, a simple approach is to use a prismatic joint with a fixed axis for synchronized actuation. Thus, as shown in Figure 4(a), a passive link serves as the actuator for the contraction DOF, enabling the three chains to perform synchronized contraction motion with the same amplitude. In Figure 4(a), the motion is verified through simulation. It is worth noting that the pipeline robot has an interaction mechanism, which contains two wheels in each limb.

Figure 4(b) shows the geometric parameters related to the connection mechanism. z_{ITS} represents the input parameter, which denotes the distance between the fixed platform and moving platform in green, and γ denotes the passive rotation parameter. The axes of revolute joints in the yellow links are always

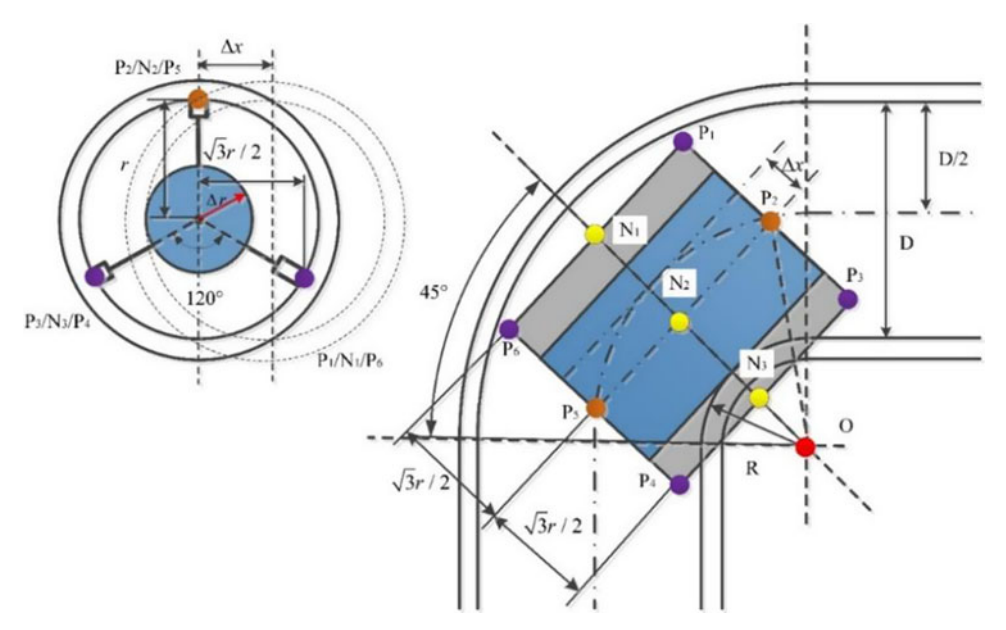


Figure 5. Topological structure.

parallel. Therefore, the following relationship can be denoted:

$$(\Delta z - z_{ITS} - L_v^a \cos(\gamma) - L_v^i)^2 + (-L_v^a \sin(\gamma))^2 = (L^p)^2$$
(6)

Eq. (6) can be rewritten as

$$\gamma = \arccos\left(\frac{(141 - z_{\text{ITS}})^2 + 3020.6025}{136.1(141 - z_{\text{ITS}})}\right) \tag{7}$$

3.2. Constraint condition analysis of elbow

Of all the pipe types, bent pipes pose the greatest constraints on pipe inspection robots. If the size of the pipe inspection robot satisfies the size constraints of the elbow, then the size of the robot allows it to pass through other types of pipes as well. Therefore, it is necessary to analyze the constraints of the pipeline inspection robot at the elbow.

This research is to design a wheeled pipeline inspection robot with three branch chains. The design goal is that the pipeline inspection robot can adapt to pipelines with a diameter of 230-300mm. At the initial position, the three branch chains of the pipeline inspection robot are symmetrically arranged at an angle of 120° to each other, and the three branch chains are identical in mechanical structure. The pipe inspection robot has the function of actively changing the diameter, which can adapt to pipes with different inner diameters. The schematic diagram of the robot at the elbow is shown in Figure 5. P_i represents the contact point between the front and rear wheels of the robot and the inner wall of the pipe. The dark blue part in Figure 5 is the main body of the robot, which will interfere with the inner wall of the pipe at the elbow. Therefore, the critical condition for the pipeline robot to be constrained can be found when the main body of the robot and the inner wall of the pipeline just interfere.

It is easy to find the relationship between the radius r of the branch chain and the diameter D of the pipeline as r = D/2. L represents the maximum length of the pipeline inspection robot along the pipeline axis, and the radius of curvature of the elbow is R. And:

$$0 < L < P_1 P_6 \tag{8}$$

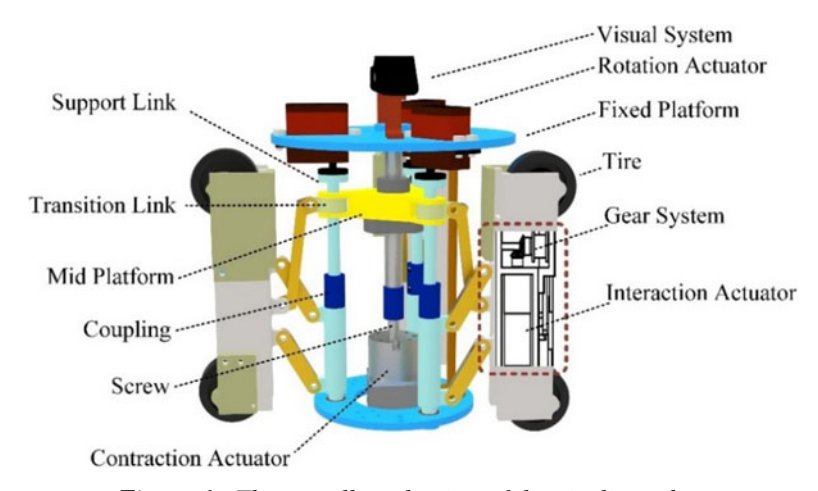


Figure 6. The overall mechanism of the pipeline robot.

where

$$P_1 P_6 = 2P_1 N_1 = 2P_2 N_2 = 2\left(OP_2^2 - ON_2^2\right)^{\frac{1}{2}} = 2\left(\left(R + \frac{D}{2}\right)\right)^2 - \left(R + \frac{D}{2} - \Delta x\right)^2\right)^{\frac{1}{2}}$$
(9)

The bending angle of the elbow is 90° , and the radius of curvature R = D/2, $\Delta x = r - \Delta r$ is the offset distance between the axis of the robot and the axis of the pipe at the elbow. $\Delta r = 80mm$ is the circumscribed circle radius of the main body of the pipeline robot. When the pipe diameter takes the minimum value. Therefore, in order to meet the design requirements that the pipeline inspection robot can work normally in the pipeline with a diameter of 230-300mm, it is necessary to ensure that the size of the pipeline inspection robot in the axial direction of the pipeline does not exceed 244mm.

3.3.3 D model of the pipeline inspection robot

In this study, the 3D model of the pipeline inspection robot was established, as shown in Figure 6. In order to facilitate the subsequent motion simulation analysis, only the necessary components are included in the assembly, and standard parts such as screws and pins that do not affect the simulation results are not displayed in the 3D model of the assembly.

As shown in Figure 7(a), the minimum length of the branch chain of the pipeline inspection robot is 212*mm* when it is fully contracted, and the maximum length is 240*mm* when the branch chain is fully expanded. Figure 7(b) shows the movement pattern A of the pipeline inspection robot in the pipeline in a symmetrical arrangement of branch chains, and Figure 7(c) shows the movement pattern B of the pipeline inspection robot in the pipeline after deformation.

4. Analysis of the steering motion of the pipeline inspection robot

4.1. Kinematic and stiffness analysis

This section first examines the kinematic relationship of the pipeline robot. Due to the symmetrical configuration of the mechanism, one of its limbs is selected for analysis. As shown in Figure 8(a), links A_1A_2 , A_2A_3 , A_3A_4 , and A_1A_4 form the four sides of a parallelogram mechanism, with points A_1 , A_2 , A_3 , and A_4 located at the centers of the respective revolute joints of the parallelogram. Point B_1 is at the midpoint of link A_2A_3 , and points B_1 and B_2 are the rotational centers of the revolute joints at the ends of link B_1B_2 . Component B_2C_2 corresponds to the slider part of a slider-crank mechanism. Additionally, link A_1A_4 can drive the branch to rotate around the axis C_1C_2 .

Based on Figure 8(a), the kinematic equations related to the end-effector can be established. A coordinate system $\{O - XYZ\}$ is set up at the center of the main body. According to the connection of the

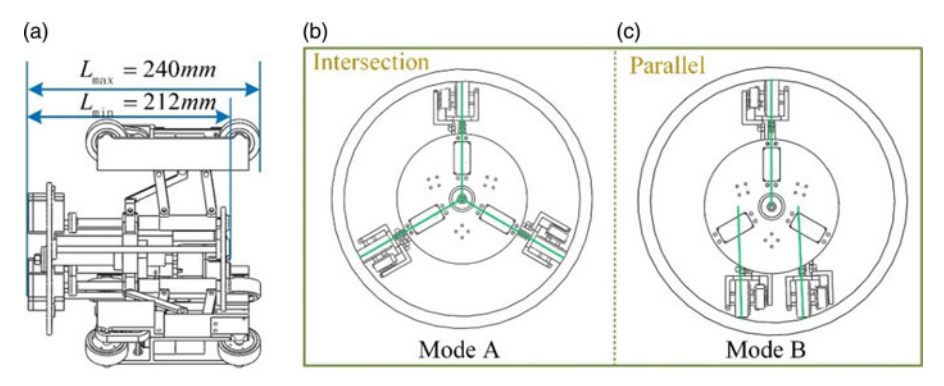


Figure 7. The 3D model and movement mode of the pipeline inspection robot: (a) Length range when contracting. (b) Movement pattern A. (c) Movement pattern B.

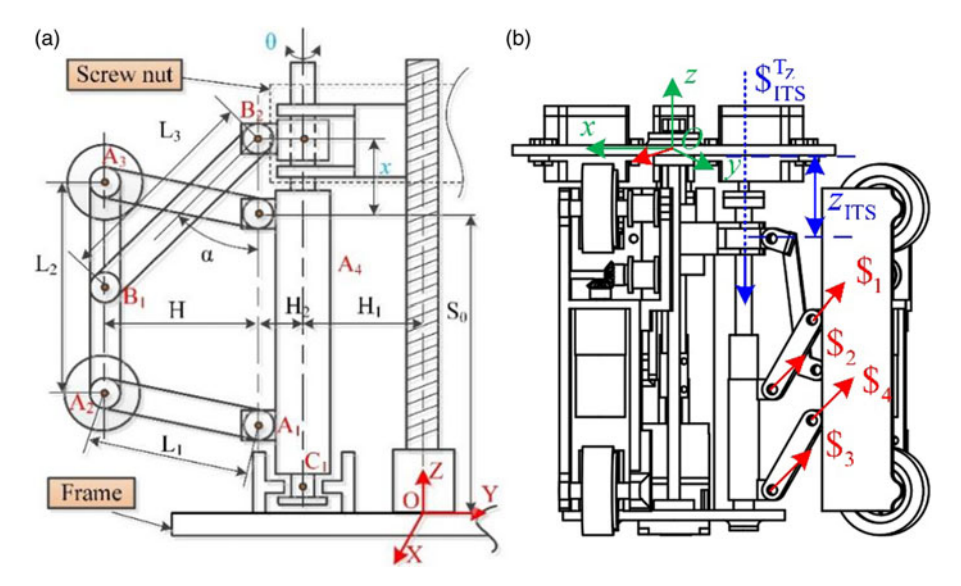


Figure 8. Schematic diagrams: (a) Dimensions of a single limb. (b) Motion screw system in each limb.

links, the mapping relationship between the coordinates of any point on link A_2A_3 in $\{O - XYZ\}$ and the driving joints can be derived. Take point B_1 , the midpoint of link A_2A_3 . In $\{O - XYZ\}$, the coordinate of B_1 is expressed as (x, y, z). Using the vector operation method, the following equations can be obtained:

$$\begin{cases}
\overrightarrow{OB_1} = \overrightarrow{OC_2} + \overrightarrow{C_2B_2} + \overrightarrow{B_2B_1} \\
\overrightarrow{OC_2} = (0 - r_2 S_0 + X)^T \\
\overrightarrow{OB_1} = \overrightarrow{OC_2} + H_1 \overrightarrow{e_{C_2B_2}} + L_3 \overrightarrow{e_{B_2B_1}}
\end{cases}$$
(10)

where $\overrightarrow{e_{C_2B_2}}$ and $\overrightarrow{e_{B_2B_1}}$ represent unit vectors, X means the distance between points B_2 and A_4 , H_1 denotes the distance between link A_1A_4 and link C_1C_2 , L_3 reflects the length of link B_1B_2 . Denote the angle between link A_1A_4 and link B_1B_2 as α , and the rotation angle of each limb as θ . The solution of forward kinematics can be obtained:

$$\begin{cases} x = H_1 \sin \theta + L_3 \sin \alpha \sin \theta \\ y = -r_2 - H_1 \cos \theta - L_3 \sin \alpha \cos \theta \\ z = S_0 + X - L_3 \cos \alpha \end{cases}$$
 (11)

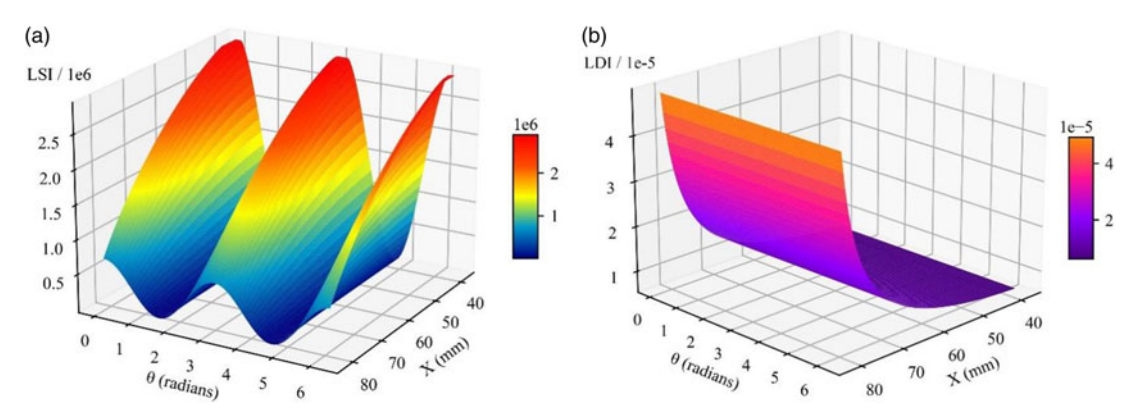


Figure 9. Performance analysis: (a) Stiffness: LSI. (b) Dexterity: LDI.

where $\cos \alpha = (L_3^2 + (L_2/2 + X)^2 - L_1^2)/(2L_3(L_2/2 + X))$. Differentiate Eq. (11) yields the Jacobian matrix J, which satisfy the relationship $(\partial X \partial \theta)^T = J(\partial x \partial y \partial z)^T$. The final Jacobian matrix can be obtained as

$$J = \frac{1}{D} \begin{pmatrix} (b^2 + d^2) a - (ab + cd) b & (b^2 + d^2) c - (ab + cd) d & (b^2 + d^2) e \\ - (ab + cd) a + (a^2 + c^2 + e^2) b & - (ab + cd) c + (a^2 + c^2 + e^2) d & - (ab + cd) e \end{pmatrix}$$
(12)

where $D = (a^2 + c^2 + e^2)(b^2 + d^2) - (ab + cd)^2$, $A = (L_2/2 + X)^2 - L_3^2 + L_1^2$, $B = 2 \sin \alpha (L_2/2 + X)^2$, $a = -A \cos \alpha \sin \theta / B$, $b = H_1 \cos \theta + L_3 \sin \alpha \cos \theta$, $c = A \cos \alpha \cos \theta / B$, $d = H_1 \sin \theta + L_3 \sin \alpha \sin \theta$, $e = \sin \alpha (A + 2L_3^2 - 2L_1^2)/B$.

Based on the calculated Jacobian matrix J, the stiffness of the mechanism can be analyzed. Generally, the stiffness matrix is often utilized to assess the local stiffness of any point in space, which can be denoted as

$$K_L = J^T K_J J \tag{13}$$

where $K_J = 1000 \, N/mm$ in this mechanism. In the same way, the local dexterity index LDI for the manipulator can be expressed as

$$LDI = \frac{1}{\left(\sqrt{\operatorname{tr}(J^{T}J)} \cdot \sqrt{\operatorname{tr}((JJ^{T}) \cdot JJ^{T})}\right)}$$
(14)

The two indices with two input parameters X and θ are shown in Figure 9. Figure 9(a) demonstrates the result of the stiffness analysis. Local stiffness (LSI) in the figure becomes larger as the value of X decreases. The overall stiffness can ensure that the pipeline robot does not undergo obvious deformation during operation. Figure 9(b) shows the result of the LDI analysis, in which the curve is smooth. Global dexterity (GDI) represents the average dexterity of the manipulator across its reachable workspace [26], calculated as the arithmetic mean of local dexterity values:

$$GDI = \frac{\int_{w} (LDI) dX d\theta}{\int_{w} dX d\theta} = 1.4 \times 10^{-5}$$
 (15)

4.2. Motion/force transmission analysis

Motion/force transmission analysis [27–29] is an essential process for evaluating the transmission efficiency of a mechanism, which includes three critical indexes, namely input transmission index (ITI), output transmission index (OTI), and local transmission index (LTI) [30]. ITI represents the transmission efficiency of each drive joint to the chain, OTI represents the transmission efficiency of the output motion of the moving platform to the chain after locking the other drive joints, and LTI represents the motion/force transmission efficiency of the entire mechanism.

For the pipeline robot designed in this paper, the revolute joint drive on the fixed platform is used to adjust the relative positions between the branches. Clearly, rotation along a circumference does not transmit force to the external environment, and analyzing its motion transmission efficiency is meaningless. Therefore, this subsection only analyzes the motion and force transmission of the synchronized contraction motion actuation.

Since the mechanism is symmetrically distributed, the motion and force transmission analysis is conducted for a single limb. The coordinate system is established as shown in Figure 8(b), with the Z-axis perpendicular to the fixed platform, the X-axis parallel to the axis of the revolute joint in the parallelogram mechanism, and the Y-axis conforming to the right-hand rule. $\$_i$, i = 1, 2..7 represent motion screws in a limb, and $\$_{TS}^{T_z}$ with a blue arrow indicates the active motion screw which corresponds to the actuation.

Suppose that the revolute joint 1 is locked. The limb can be considered as a sub-parallel mechanism that contains three branches. Motion screws in each branch can be obtained by screw theory:

$$\$_{branch1} = \begin{cases} \$_{z_{ITS}} = (0\ 0\ 0;\ 0\ 0\ 1)^{T} \\ \$_{2} = (1\ 0\ 0;\ 0\ -z_{ITS}\ -15)^{T} \\ \$_{3} = (1\ 0\ 0;\ 0\ -z_{ITS}\ -68.05\cos(\gamma)\ -15\ -68.05\sin(\gamma))^{T} \end{cases}$$
(16)

$$\$_{branch2} = \begin{cases} \$_4 = (1\ 0\ 0;\ 0\ -116\ -15)^T \\ \$_5 = (1\ 0\ 0;\ 0\ -z_{ITS} + 25\ -68.05\cos(\gamma)\ -15\ -68.05\sin(\gamma))^T \end{cases}$$
(17)

$$\$_{branch3} = \begin{cases} \$_6 = (1\ 0\ 0;\ 0\ -z_{TS} - 25 - 68.05\cos(\gamma)\ -15 - 68.05\sin(\gamma))^T \\ \$_7 = (1\ 0\ 0;\ 0\ -166\ -15)^T \end{cases}$$
(18)

The final constraint screw systems and motion screw system corresponding the interaction platform can be obtained by using reciprocal product from Eq. (16), (17) and (18):

$$\begin{cases} \$_{1}^{r} = (0\ 0\ 0; 0\ 1\ 0)^{T} \\ \$_{2}^{r} = (0\ 0\ 0; 0\ 0\ 1)^{T} \\ \$_{3}^{r} = (1\ 0\ 0; 0\ 0\ 0)^{T} \\ \$_{4}^{r} = (0\ 68.05\sin(\gamma)\ 141 - z_{ITS} - 68.05\cos(\gamma); l_{4}\ 0\ 0)^{T} \\ \$_{5}^{r} = (0\ 68.05\sin(\gamma)\ 141 - z_{ITS} - 68.05\cos(\gamma); l_{5}\ 0\ 0)^{T} \\ = 15z_{TR} = 1021\cos(\gamma) + 11276\sin(\gamma) l_{5} = 2115 - 15z_{TR} = 1021\cos(\gamma) + 7894 \end{cases}$$

where $l_4 = 2115 - 15z_{\text{TTS}} - 1021\cos(\gamma) + 11276\sin(\gamma), l_5 = 2115 - 15z_{\text{TTS}} - 1021\cos(\gamma) + 7894\sin(\gamma).$

$$\$_{OTS} = (0\ 0\ 0; 0\ 141 - z_{ITS} - 68.05\cos(\gamma) - 68.05\sin(\gamma))^{T}$$
(20)

According to Eq. (20), the output motion screw is equivalent to the motion created by the parallelogram mechanism, which is a translational DOF. After analyzing the DOF of the mechanism, the motion and force transmission can be obtained. The index has been divided into two parts, input transmissibility and output transmissibility [30]:

$$\begin{cases} \eta_{ITI} = |\$_{ITS}^{\circ}\$_{TWS}|/|\$_{ITS}^{\circ}\$_{TWS}|_{max} \\ \eta_{OTI} = |\$_{OTS}^{\circ}\$_{TWS}|/|\$_{OTS}^{\circ}\$_{TWS}|_{max} \end{cases}$$
(21)

where $\$_{TWS}$ represents the transmission wrench screws. By removing the active joint $\$_{ITS}$, the additional wrench screw can be calculated, which can be viewed as $\$_{TWS}$:

$$\$_{TWS} = (0 \sin(\gamma) - \cos(\gamma); 15 \cos(\gamma) - z \sin(\gamma) \ 0 \ 0)^{T}$$
 (22)

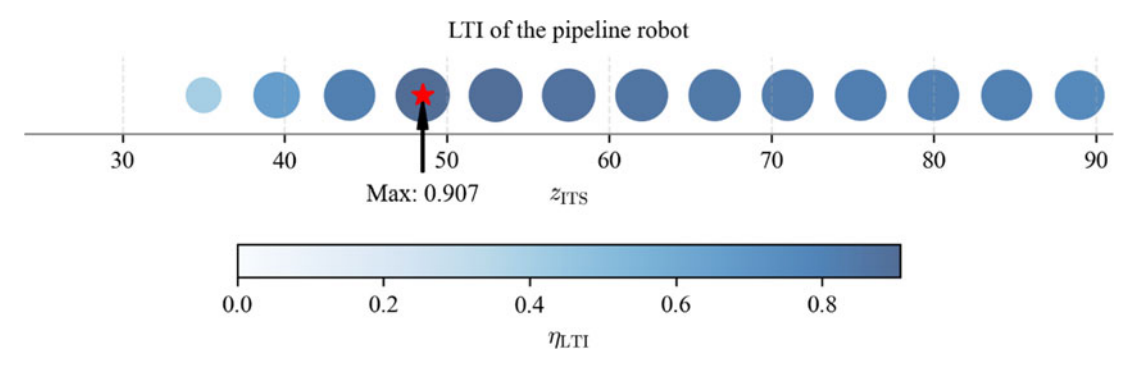


Figure 10. LTI of the z_{ITS} input.

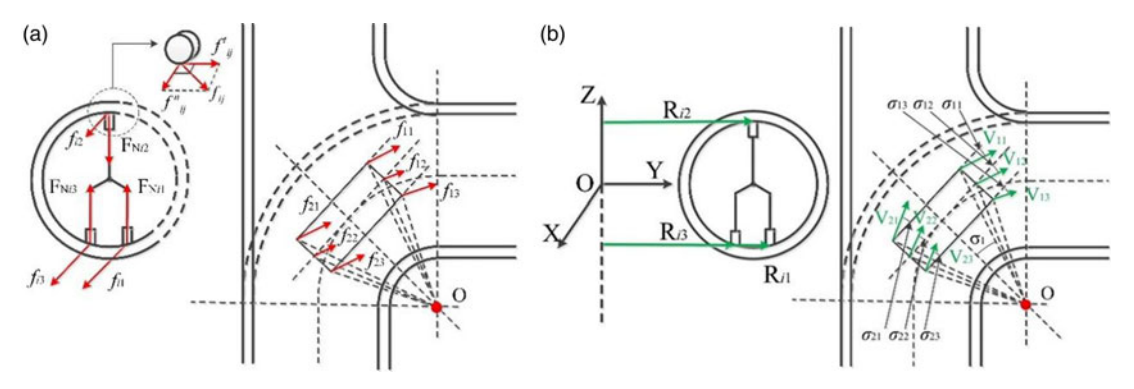


Figure 11. (a) Velocity analysis of steering motion. (b) Force analysis of steering movement.

Combine Eq. (20), (21), and (22):

$$\begin{cases} \eta_{ITI} = |\cos(\gamma)| \\ \eta_{OTI} = |(141 - z_{ITS})\sin(\gamma)| / |(141 - z_{ITS})\sin(\gamma)|_{max} \end{cases}$$
 (23)

Since the overall motion/force transmissibility depends on the minimum of the two, LTI can be expressed as [30]

$$\eta_{ITI} = \min\left(\eta_{ITI}, \eta_{OTI}\right) \tag{24}$$

Substitute Eq. (7) into (23) and (24), the following LTI can be obtained:

$$\eta_{\text{LTI}} = \min \left(\left| \frac{\left(141 - z_{\text{ITS}}\right)^2 + 3021}{136.1 \left(141 - z_{\text{ITS}}\right)} \right|, \frac{\sqrt{-\left(141 - z_{\text{ITS}}\right)^4 + a\left(141 - z_{\text{ITS}}\right)^2 - b}}{40.087\sqrt{c}} \right)$$
(25)

where a = 12482.005, b = 9124060.75, c = 18523. Figure 10 shows the LTI of the mechanism with z_{ITS} changing. The LTI value always remains large as the input changes, indicating that the mechanism can maintain high stiffness within a large pipe radius range.

4.3. Velocity analysis of the steering motion of the pipeline inspection robot

As shown in Figure 11(a), the coordinate system $\{O - XYZ\}$ is established with the center of curvature of the elbow as the coordinate origin. The motion of the robot passing through the elbow pipe and the branch pipe at a constant speed is equivalent to the uniform circular motion around the rotation center point O. The angular velocity of the pipeline inspection robot around the point O is ω , and the ratio of the speed of each driving wheel to the contact point of the pipeline can be obtained as

$$V_{i1} \colon V_{i2} \colon V_{i3} = R_{i1} \colon R_{i2} \colon R_{i3} = \left(a_{i1}^2 + b_{i1}^2\right)^{\frac{1}{2}} \colon \left(a_{i2}^2 + b_{i2}^2\right)^{\frac{1}{2}} \colon \left(a_{i3}^2 + b_{i3}^2\right)^{\frac{1}{2}} \tag{26}$$

where

$$\begin{cases}
a_{i1} = R + \frac{D}{2} + \frac{\Delta r}{2} \\
a_{i2} = R + \frac{D}{2} \\
a_{i3} = R + \frac{D}{2} - \frac{\Delta r}{2} \\
b_{i1} = b_{i2} = b_{i3} = \frac{L}{2}
\end{cases}$$
(27)

And the speed of each driving wheel can be obtained as

$$v_{ij} = V_{ij} cos \delta_{ij} \tag{28}$$

where $tan\delta_{ij} = a_{ij}/b_{ij}$, i = 1, 2 represents the front and rear wheels of the robot, and j = 1, 2, 3 represents the j-th wheel at the front and rear.

4.4. Force analysis of the steering motion of the pipeline inspection robot

When moving in the curved pipe, the robot is constrained by the inner wall of the pipe, and there is no need to consider the situation where the centripetal force is greater than the frictional force. But at the T-branch, if the steering speed is too high and the friction force is smaller than the centripetal force, the pipeline inspection robot will overturn and get stuck. Therefore, it is necessary to analyze the force of the pipeline inspection robot during the steering movement. Figure 11(b) shows the force situation of the robot when it is cornering. Assuming that the T-branch is located on the horizontal plane, the centripetal force experienced by the robot when turning is

$$F_n = m\omega^2 (R + D/2) \tag{29}$$

Considering only the rolling motion of the driving wheel, the static friction force on the robot is

$$f_{ij}^{total} = \sum_{i=1}^{2} \sum_{j=1}^{3} f_{ij} = \mu \sum_{i=1}^{2} \sum_{j=1}^{3} F_{N_{ij}} = \mu (mg + F_p)$$
(30)

where F_p represents the total tightening force of the robot on the pipe wall. The following conditions need to be met for the robot not to overturn during the steering movement:

$$F_n < \sum_{i=1}^2 \sum_{j=1}^3 f_{ij}^n = \left(\left(f_{ij}^{total} \right)^2 - \left(\sum_{i=1}^2 \sum_{j=1}^3 f_{ij}^t \right)^2 \right)^{\frac{1}{2}}$$
 (31)

Substitute (29) and (30) into (31):

$$m\omega^{2}(R+D/2) < \left(\left(m\left(mg+F_{p}\right)\right)^{2} - \left(\sum_{i=1}^{2}\sum_{j=1}^{3}f_{ij}^{t}\right)^{2}\right)^{\frac{1}{2}}$$
 (32)

Simplify the (32) to obtain the relationship between the angular velocity ω of the steering motion and the tightening force as follows:

$$\omega < \left[\left(m^2 \left(mg + F_p \right)^2 - \left(\sum_{i=1}^2 \sum_{j=1}^3 f_{ij}^t \right)^2 \right) / \left(m \left(R + D/2 \right) \right) \right]^{\frac{1}{4}}$$
 (33)

According to (33), the pipeline detection robot can pass through the T-branch smoothly by adjusting the angular velocity ω or F_p of the steering movement. Where f_{ij} is the friction force of a single driving wheel, f_{ij}^n represents the component force of the friction force on the driving wheel in the tangential direction of the wheel, and f_{ij}^n is the component force of the friction force on the driving wheel in the normal direction of the wheel.

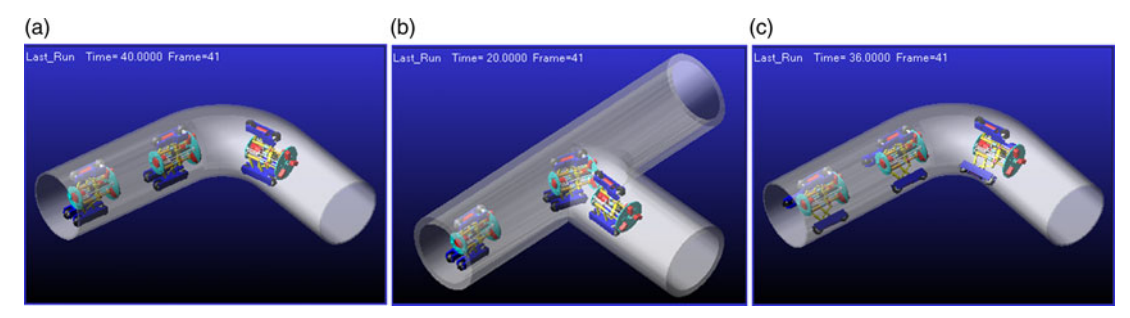


Figure 12. Simulation of pipeline inspection robot:(a) Mode a in the elbow. (b) Mode B in the elbow. (c) Mode B in the T-branch.

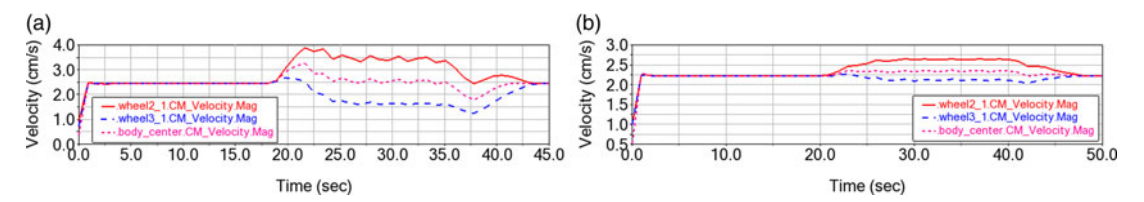


Figure 13. Turning speed in two modes: (a) Velocity analysis of mode A. (b) Velocity analysis of mode B.

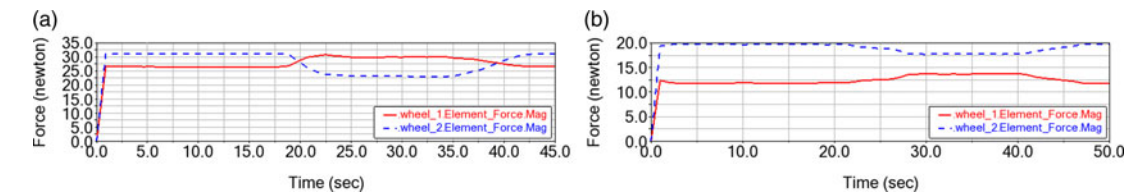


Figure 14. Contact forces: (a) Mode A. (b) Mode B.

5. Pipeline inspection robot steering motion simulation

The 3D model of the robot is imported into the simulation software for kinematics simulation. Figure 12 shows the movement process of the pipeline inspection robot through the elbow and T-branch. Figure 13 shows the kinematics simulation results obtained by the pipeline detection robot passing through the elbow in two motion modes. Figure 13(a) shows the pipeline inspection robot passing through the elbow in mode A, and Figure 13(b) shows the pipeline inspection robot passing through the elbow in mode B. From Figure 13, it can be concluded that given the different rotational speeds of the driving wheels, when moving in a straight pipe, the actual moving speed of each wheel is the same and equal to the moving speed of the center of the robot. After entering the elbow, the constraints of the pipe on the wheels have changed, and the difference in the output speed of the wheels is reflected at this time. The ratio of the velocities of the inner and outer wheels in the elbow is the same as that analyzed in (26).

The above situation shows that due to the speed difference between the inner and outer sides of the straight pipe, the wheels slipped. To avoid energy waste and tire wear caused by wheel slippage, in practical applications, the wheel speed is distributed according to the analysis in (26) at the elbow, and the wheel speed is controlled to be the same in the straight pipe.

Figure 14 shows the simulation results of the contact force between the wheels and the inner wall of the pipeline when the pipeline inspection robot moves in the horizontal elbow. Under the same conditions, in mode A, the outer wheel $(wheel_1)$ receives a resultant force of 31N in the straight pipe and 23N at the elbow; the inner wheel $(wheel_2)$ receives a resultant force of 27N in the straight pipe and 30N at the elbow. In mode B, the outer wheel $(wheel_1)$ receives a resultant force of 20N in the straight pipe and 16.5N in the elbow; the inner wheel $(wheel_2)$ receives a resultant force of 12N in the straight pipe and

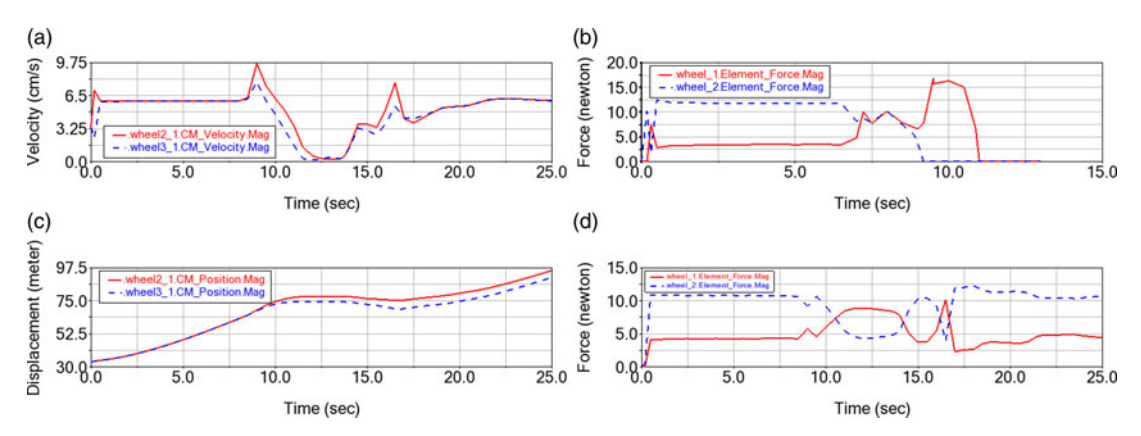


Figure 15. Active steering movement in the T-branch: (a) Velocity. (b) Contact force. (c) Displacement. (d) Contact force.

13N in the elbow. On the whole, the force on the wheels of the pipeline inspection robot in mode A is greater than that in mode B.

Steering the movement of pipeline inspection robots in the T-branch has been very difficult. This is because a single-module pipeline inspection robot cannot find contact points, and the robot will get stuck in the T-branch. In theory, the pipeline inspection robot proposed in this paper can realize the active steering movement in the T-branch by the differential motion of the inner and outer wheels in the case of mode B. Also, in the motion simulation software, active steering movement is realized by adjusting the differential movement of the inner and outer wheels. Figure 15(a) shows that when the pipeline inspection robot enters the T-branch interface, the speed changes greatly, but the inner and outer wheels still maintain a certain speed difference. Compared with the speed change in Figure 15(b), the speed change is larger. Figure 15(c) shows the pipeline inspection robot starts to enter the T-branch at 10s and leaves the T-branch at 17s. The simulation results show that the pipeline inspection robot realizes the turning motion at the T-branch by the differential motion of the inner and outer wheels. But the whole moving process is not a continuous, uniform circular motion, as the environment of the inner wall of the pipe at the T-branch is far more complex than that of the elbow. And it is an uneven surface, which hinders the robot's steering movement.

According to (33), when the steering speed of the pipeline inspection robot is too high and the friction force it receives is less than its centripetal force, the pipeline inspection robot will overturn when passing the T-branch, and Figure 15(d) also confirms this point.

6. Experiment validation

6.1. Development of a pipeline robot prototype

The control system of the pipeline robot is shown in Figure 16. The entire system includes an Arduino board, a stepper motor driver, a servo control board, a stepper motor, three DC motors, and three servos. The control system is powered by a DC power supply, specifically a 24 V lithium battery. Since the Arduino board, motor drivers, and various motors require different voltages, multiple buck modules are used to reduce the power supply voltage.

Although the Arduino board has sufficient interfaces to control the entire system, experiments reveal that when multiple interfaces are connected to the Arduino board simultaneously, the board is prone to being overloaded. Therefore, a servo control board is used to drive the three servos, while the Arduino board is responsible for controlling the stepper motor and DC motors. Furthermore, this study also employs a four-channel L298N driver to control the three DC motors.

The pipeline robot prototype is shown in Figure 16. To facilitate real-time observation of the pipeline's internal conditions, an Intel D435i depth vision camera is arranged on top. The camera can

ParametersIndexOverall Weight2.25 kgDiameter Adaptation Range230–300 mmOverall Height250–270 mm

Table II. Dimensional parameters.

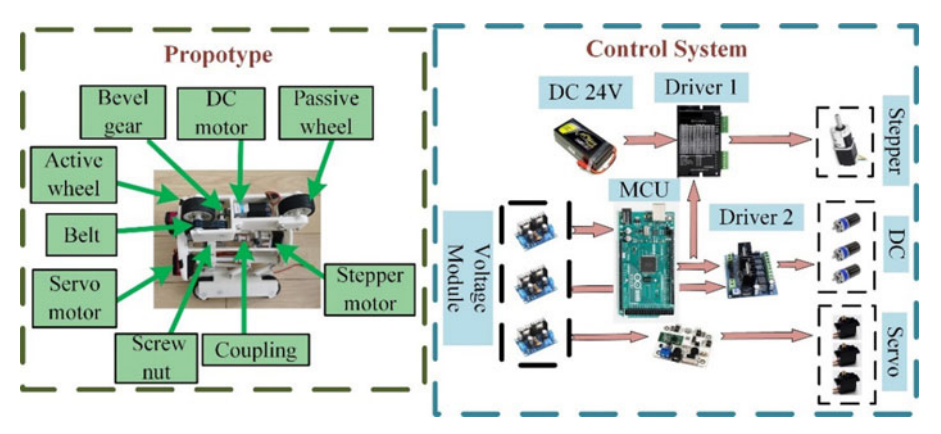


Figure 16. Prototype of the pipeline robot.

generate depth images even in dark environments. In this study, the IMU aids in measuring real-time pose information of the robot, allowing for real-time adjustments to its position. The robot's dimensional parameters are listed in Table II.

6.2. Function verification

Straight pipes are common in pipeline systems, and navigating through them is the simplest task for a pipeline robot. To verify the capability of the pipeline robot crawling in a straight pipe, a transparent acrylic pipe with an inner diameter of 290mm is selected and placed horizontally and vertically. The test of the pipeline robot in a straight pipe is shown in Figure 17. During crawling, the angles between limbs are constant. The time required for the robot to crawl 30 cm is recorded using a watch, and five repeated experiments are conducted. The corresponding data are shown in Table III. The result shows that the average speed of the robot in the horizontal pipe is 26.5 cm/s, verifying that the speed of the robot in the straight pipe meets the design target of 20 cm/s. Meanwhile, the speed of the robot in the vertical pipe can achieve an average velocity of 23.4 cm/s, overcoming its own weight. Multiple tests demonstrated that the pipeline robot can successfully crawl through the straight pipe.

The proposed pipeline robot can also travel in a bent pipe, which is given in Figure 18. The inner radius of the pipe is 300mm, and the radius of this 90° curvature is also 300mm. In order to achieve steering movement, a special velocity relationship should be satisfied, as shown in Figure 18. The experiments verify that the robot can successfully travel through this bent pipe, and the wheels are always in contact with the inner wall of the pipe during this process.

7. Conclusions

In this paper, a novel pipeline inspection robot was designed. First, a four-degree-of-freedom pipeline robot is introduced using numerical synthesis and graph synthesis. Choose V = 7, No. 20 as the result of numerical synthesis and the 18-th topological graph in the arrangement HQTQTQ as the result of graph synthesis. The coupling mid-platform is inspired by a parallelogram mechanism, and then the overall pipeline mechanism is introduced, which can achieve synchronized contraction motion. Kinematic

		2 3			
State	No.	v(cm/s)	State	No.	v(cm/s)
Horizon	1	25.5	Vertical	1	23.5
	2	26.7		2	23.4
	3	27.9		3	24.0
	4	25.2		4	24.1
	5	27.1		5	22.0

Table III. Velocity for the robot to crawl 30cm.

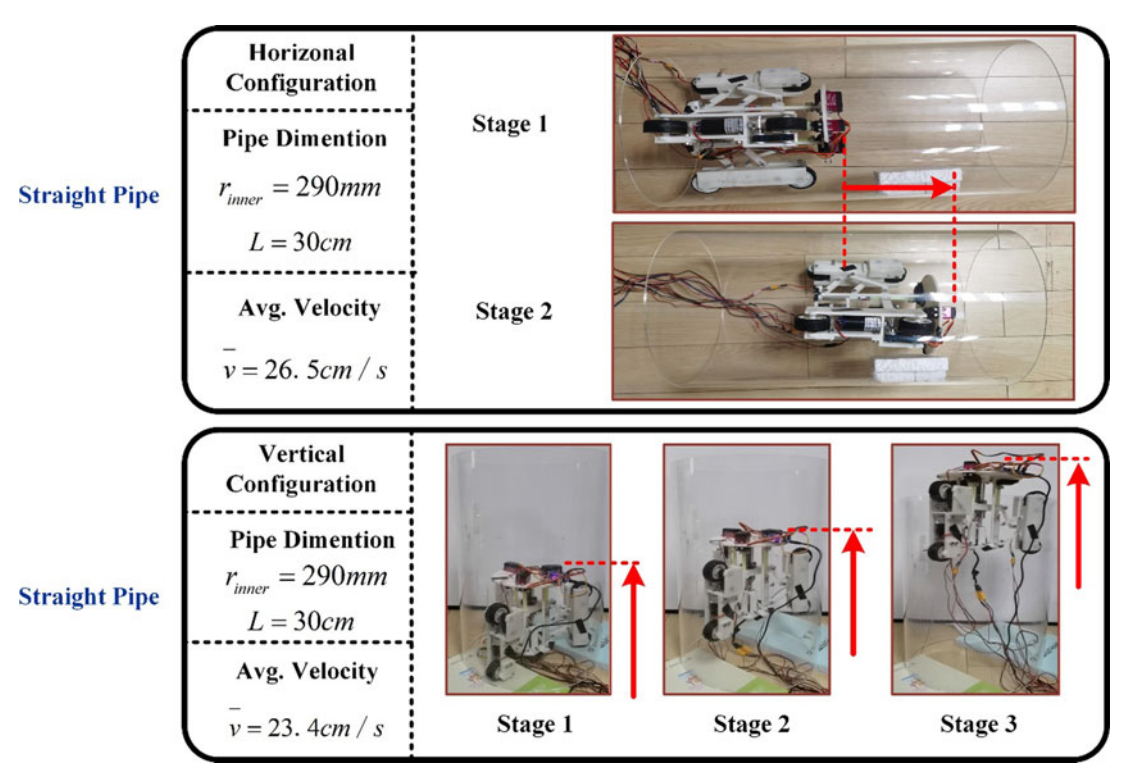


Figure 17. Experiments in a straight pipe.

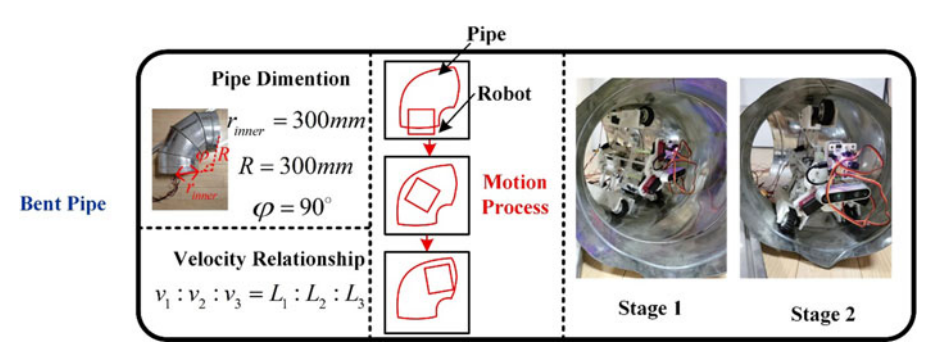


Figure 18. Experiments in a bent pipe.

closed-loop equations of the mechanism are established, and performance analysis, including stiffness and dexterity, is conducted based on the Jacobian matrix. Meanwhile, the motion and force transmission characteristics are analyzed through screw theory. Suppose the input value between 26mm and 89mm, the maximum value of LTI is 0.907, indicating that the mechanism possesses good force transmission

ability. And the speed and contact force of the robot are also calculated. The two motion modes of the robot through the elbow are simulated, and the simulation results are combined to compare the two motion modes. Finally, simulation verification is carried out for the proposed method of crossing the T-branch. The simulation results show that the robot can realize active steering in the T-branch. Finally, three occasions are chosen to verify its value, including a straight pipe with horizontal configuration, a straight pipe with vertical configuration, and a bent pipe. The average velocity in a straight pipe with horizontal and vertical configurations is 26.5 cm/s and 23.4 cm/s, respectively. And it can successfully travel through a bent pipe with 90° . In the future, the prototype of the pipeline inspection robot will be developed and applied in the inspection and maintenance of oil pipelines, natural gas pipelines, and drainage pipelines.

Author contributions. Yongheng Xing: Validation, methodology, and formal analysis; Weizhan Ma: Investigation, validation, and formal analysis. Chunxu Tian: Visualization, supervision, and resources; Dan Zhang: Writing–review & editing, supervision, and conceptualization.

Financial support. This work was funded by the National Nature Science Foundation of China (grants 52305012), the Research Institute for Artificial Intelligence of Things (RIAIOT), Research Institute for Intelligent Wearable Systems (RI-IWEAR), Research Institute for Advanced Manufacturing (RIAM), and Research Centre of Textiles for Future Fashion (RCTFF) at the Hong Kong Polytechnic University.

Competing interests. The authors declare that they have no known competing financial interests or personal relationships that could have appeared to influence the work reported in this paper.

Ethical approval. Not applicable.

References

- [1] O. Tătar, C. Cirebea, A. Alutei and D. Mândru, "The Design of Adaptable Indoor Pipeline Inspection Robots," In: 2010 IEEE International Conference on Automation, Quality and Testing, Robotics (AQTR) (IEEE, 2010) pp. 1–4.
- [2] Z. Shen, M. Xie, Z. Song and D. Bao, "Design and performance analysis of a parallel pipeline robot," *Electronics* 13, 4848 (2024)
- [3] J. Gallardo-Alvarado, "A Gough-Stewart parallel manipulator with configurable platform and multiple end-effectors," *Meccanica* 55, 597–613 (2020).
- [4] M. M. Horoub, M. Hassan and M. A. Hawwa, "Workspace analysis of a Gough-Stewart type cable marine platform subjected to harmonic water waves," *Mech. Mach. Theory* 120, 314–325 (2018).
- [5] C. Tian, D. Zhang, H. Tang and C. Wu, "Structure synthesis of reconfigurable generalized parallel mechanisms with configurable platforms," *Mech. Mach. Theory* **160**, 104281 (2021).
- [6] X. Jin, Y. Fang and D. Zhang, "Design of a class of generalized parallel mechanisms with large rotational angles and integrated end-effectors," *Mech. Mach. Theory* 134, 117–134 (2019).
- [7] L. Wang, Y. Fang and L. Li, "Design and analysis of the gripper mechanism based on generalized parallel mechanisms with configurable moving platform," *Front. Mech. Eng.* **16**(4), 1–17 (2021).
- [8] Y. Xing, C. Tian, Z. Xia, J. Gu and D. Zhang, "The novel synthesis of generalized parallel manipulators with 8R Kirigamiinspired configurable platform," *Mech. Mach. Theory* 209, 106003 (2025).
- [9] B.-J. Yi, H. Y. Na, J. H. Lee, Y.-S. Hong, S.-R. Oh, I. H. Suh and W. K. Kim, "Design of a parallel-type gripper mechanism," Int. J. Robot. Res. 21, 661–676 (2002).
- [10] C. Tian, Y. Fang and Q. J. Ge, "Structural synthesis of parallel manipulators with coupling sub-chains," *Mech. Mach. Theory* **118**, 84–99 (2017).
- [11] D. Archangeli, B. Ortolano, R. Murray, L. Gabert and T. Lenzi, "A lightweight powered hip exoskeleton with parallel actuation for frontal and sagittal plane assistance," *IEEE Trans. Robot.* 41, 1711–1727 (2025).
- [12] S.R. Company, "Design of a Dextrous Hand for Advanced CLAWAR Applications," **In:** *Proc. 6th Int. Conf* (Climbing Walking Robots, Citeseer, 2003) pp. 17–19.
- [13] E. F. Fichter, "A Stewart platform-based manipulator: General theory and practical construction," *Int. J. Robot. Res.* **5**, 157–182 (1986).
- [14] M. Tavakoli, L. Marques and A. T. de Almeida, "Development of an industrial pipeline inspection robot," *Ind. Robot: An International Journal* 37, 309–322 (2010).
- [15] S.-g. Roh and H. R. Choi, "Differential-drive in-pipe robot for moving inside urban gas pipelines," *I Trans. Robot.* **21**, 1–17 (2005).

- [16] H. Li, R. Li, J. Zhang and P. Zhang, "Development of a pipeline inspection robot for the standard oil pipeline of China national petroleum corporation," *Applied Sciences* 10(8), 2853 (2020).
- [17] H. M. Kim, J. S. Suh, Y. S. Choi, T. D. Trong, H. Moon, J. Koo, S. Ryew and H. R. Choi, "An In-pipe Robot with Multi-axial Differential Gear Mechanism," In: IEEE/RSJ International Conference on Intelligent Robots and Systems (IEEE, 2013) pp. 252–257.
- [18] N. S. Roslin, A. Anuar, M. F. A. Jalal and K. S. M. Sahari, "A review: Hybrid locomotion of in-pipe inspection robot," Procedia Eng. 41, 1456–1462 (2012).
- [19] I. N. Ismail, A. Anuar, K. S. M. Sahari, M. Z. Baharuddin, M. Fairuz, A. Jalal and J. M. Saad. "Development of in-pipe inspection robot: A review," In: 2012 IEEE conference on sustainable utilization and development in engineering and technology (STUDENT), IEEE (IEEE, 2012) pp. 310–315.
- [20] Y.-S. Kwon, B. Lee, I.-C. Whang and B.-J. Yi, "A pipeline inspection robot with a linkage type mechanical clutch," In: 2010 IEEE/RSJ International Conference on Intelligent Robots and Systems (IEEE, 2010) pp. 2850–2855,
- [21] S. Sakamoto, F. Hara, H. Hosokai, H. Kinoshita and Y. Abe, "Parallel-link robot for pipe inspection," In: 31st Annual Conference of IEEE Industrial Electronics Society, 2005. IECON 2005 (IEEE, 2005) pp. 6.
- [22] C. Tian, Y. Fang and Q. J. Ge, "Design and analysis of a partially decoupled generalized parallel mechanism for 3T1R motion," Mech. Mach. Theory 140, 211–232 (2019).
- [23] Z. Xia, C. Tian, Y. Xing, J. Gu, L. Li and D. Zhang, "The novel synthesis method of decoupled generalized parallel mechanisms based on motion transmission," *Mech. Mach. Theory* 210, 106019 (2025).
- [24] Z. Xia, D. Zhang, Y. Chen, C. Tian, J. Liu and C. Wu, "A novel 6 DOFs generalized parallel manipulator design and analysis based on humanoid leg," *Mech. Mach. Theory* **176**, 105029 (2022).
- [25] J. Wu, L. Zeng, Q. Ruan, J. Guo, H. Yang, L. Jing and Y.-A. Yao, "Reconfiguration and compensation design method for single-DoF closed-chain leg mechanism," *Mech. Mach. Theory* 204, 105834 (2024).
- [26] Z. Gao and D. Zhang, "Performance analysis, mapping, and multiobjective optimization of a hybrid robotic machine tool," IEEE Trans. Ind. Electron. 62, 423–433 (2014).
- [27] Q. Meng, X.-J. Liu and F. Xie, "Design and development of a Schönflies-motion parallel robot with articulated platforms and closed-loop passive limbs," *Robot. Cim-INT Manuf* 77, 102352 (2022).
- [28] L. Xu, W. Ye and Q. Li, "Evaluation method and performance indices for the motion/Force constrainability of overconstrained parallel manipulators without actuation redundancy," J. Mech. Robot. 17, 061007 (2025).
- [29] X. Jin, W. Ye and Q. Li, "New indices for performance evaluation of cable-driven parallel robots: Motion/force transmissibility," Mech. Mach. Theory 188, 105402 (2023).
- [30] J. Wang, C. Wu and X.-J. Liu, "Performance evaluation of parallel manipulators: Motion/force transmissibility and its index," Mech. Mach. Theory 45, 1462–1476 (2010).